

Title: Design Proposal: Si Photonics Circuits

Author: Josh Myers (jmyers1_chess)

I. INTRODUCTION

There is a great deal of interest in using silicon photonic circuits as a method for rapid data transfer [1]. These photonic circuits consist of many passive components, such as waveguides, Y-Branch splitters, and grating couplers. Waveguides are of particular interest, as one can learn valuable things about the effective behaviour of a waveguide mode through measuring the phase difference between two signals after being guided some distance (characteristic of the function of the given optical circuit) after passing through a beam splitter (such as a Y-Branch component). Though it is beyond the scope of this proposal to get into the physics behind real-world Y-Branch components, we will characterize their simulated behaviour at the wavelengths of interest for this design proposal (1500-1600nm). The transmission of light through a silicon core, SiO_2 waveguide is an aspect that commercial eigensolvers (Maxwell's PDEs) such as Ansys Lumerical MODE have been dedicated to modelling accurately, provided with many customizable inputs such as waveguide geometry, wavelength range, and dispersive refractive index models for the materials. Coming out of this analysis of eigenmode solutions for the propagating wave are the quasi-transverse electric (E-fields) and quasi-transverse magnetic (H-fields) wave modes; under specific conditions, waveguides can support one or more of these modes simultaneously. The wave travels in both the silicon core and the SiO_2 cladding - in the cladding, (for the dominant quasi-TE mode) the amplitude of the wave decays as it propagates away from the planar interface between the core and cladding of the strip waveguide. The strip silicon-on-insulator (SOI) waveguide (considered for this course project design) is typically fabricated on a silicon substrate, where SiO_2 buried oxide (BOX) is deposited first, then Si- SiO_2 (waveguide and cladding) interface is deposited using etching and electron beam lithography with a characteristic sidewall roughness (which plays an important role in the emergence of loss during the wave guiding process). From a phenomenological perspective, SOI waveguide designs are popular because they generally represent low loss systems (total internal reflection, which is only possible in high index materials confined by an interface with a material of a lower index of re-

fraction), where constructive and destructive interference dictate which modes emerge in the optical system (such as when the waveguide is part of an photonic circuit such as an interferometer). Then, the upper cladding of SiO_2 is deposited. Industry standards for the height of the waveguide is about 220nm - this is a fabrication constraint at the foundry for this project as well. One of the reasons for this standard is because the limited height of the waveguide allows for a limited number of modes to be guided by the waveguide, which is critical for many applications, such as in telecommunications (wavelength division multiplexing applications) [2].

In addition to the waveguide, another very important component of the optical circuit for this project is the Mach-Zehnder Interferometer (MZI), which is a single input, multiple output interferometer that involves two 50/50 beam splitters (such as Y-Branches). The operational configuration (which can be simulated in Lumerical Interconnect using the compact model library provided by this course) involves one beam splitter separating a single input into two outputs, which are then both passed through waveguides of different lengths, and then the signals are passed through the second beam splitter at (for idealization sake, perhaps) 90 degree angles to one another. Then, the two output signals are detected (at 90 degrees from one another) with wave properties (such as gain, transmission, and free spectral range) characteristic to the constructive and destructive interference of the two signals incident on the *second* beam splitter. For the purposes of this project, these two signals will experience a phase change due to the design of waveguides differing in length (as well as in general real-world applications, differing refractive indices between the two waveguides). There is also loss that is characteristic of the optical components such as the non-ideal Y-Branch, the grating couplers, and the non-idealities of the waveguides. In the next section, we will lay out some basic modelling principles for these optical circuit components, making use of Lumerical MODE solutions and Lumerical Interconnect, as well as MATLAB fittings and mathematical expressions modelling the system. We will outline the manufacturing process (electron beam lithography) at the Applied NanoTools foundry, including a monte carlo analysis of the expected outcomes with consideration to manufacturing

variation in waveguide dimensioning and effective index. Then, we will carry out curve fitting to analyse the experimental results with the aim of extracting the group index of the silicon waveguide used in the various optical circuits. A discussion of the experimental results and their comparison to simulation will follow.

II. THEORY AND SIMULATION

Consider the compact model of the waveguide - a fitted, 2nd-order Taylor series expansion for the change in effective index characteristic to the given waveguide mode:

$$n_{\text{eff}}(\lambda) = \sum_{i=0}^2 \frac{1}{i!} \frac{d^i n_{\text{eff}}(\lambda_o)}{d\lambda^i} (\lambda - \lambda_o)^i \quad (1)$$

In this case, the derivative coefficients are independent of wavelength, and depend on the waveguide geometry. While we fix the height of the waveguide to be nominally about 220nm, the width of the waveguide can be varied. For this project, we will keep the width of the waveguide to be nominally 500nm. Let's consider the two main waveguide modes - quasi-TE and quasi-TM modes. The dominant TE mode in 3 dimensional waveguides has limited electric field in the direction of propagation (though is not “pure” as in the 2-dimensional case), while the dominant TM mode has limited magnetic field in the direction of propagation. Provided in Figure 1 to Figure 4 are spatial profiles of the Lumerical MODE solutions for a waveguide of 220nm height and 500nm width at a wavelength of 1550nm, with a cladding of 4um by 4um cross-section. The color scale is that of the time average intensity of the fields. As can be seen in these

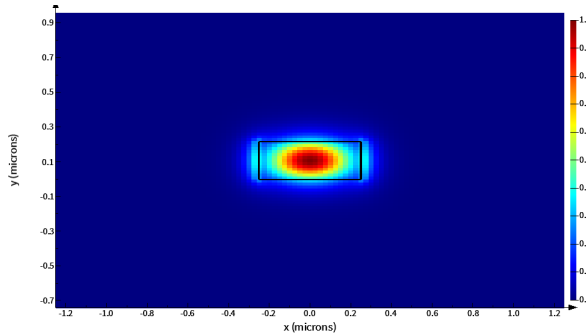


Fig. 1: The dominant quasi-TE mode for a strip waveguide with width 500nm and height 220nm at 1550nm.

spatial profiles of the Lumerical MODE simulation of the waveguide modes, the dominant TE mode is the only mode that is largely confined to the inside of the strip waveguide when width is 500nm. This idea makes this waveguide simple to investigate, as only one effective refractive index plays a dominant role in dictating the waveguide properties in the MZI setup. Of course, it is

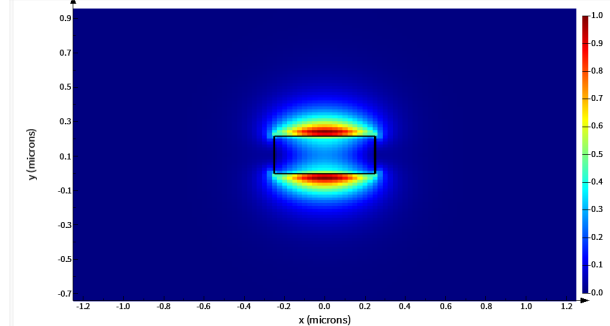


Fig. 2: The dominant quasi-TM mode for a strip SOI waveguide with width 500nm and height 220nm at 1550nm.

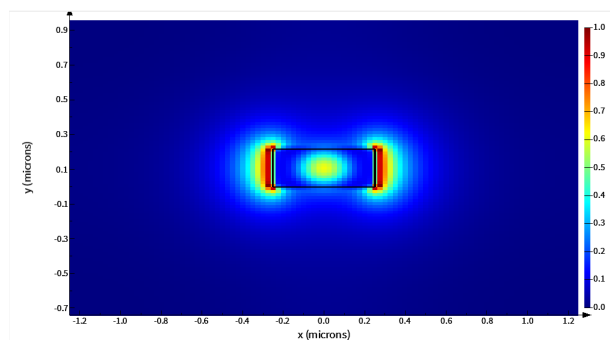


Fig. 3: The second quasi-TE mode for a strip SOI waveguide with width 500nm and height 220nm at 1550nm.

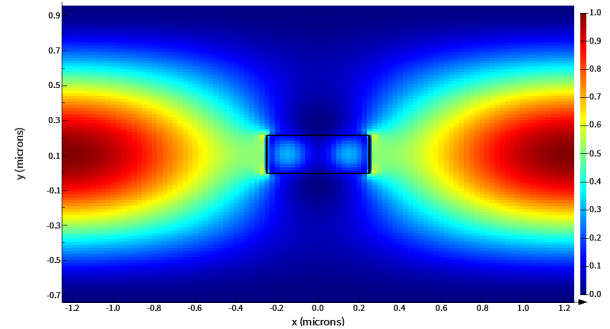


Fig. 4: The third quasi-TE mode for a strip SOI waveguide with width 500nm and height 220nm at 1550nm.

important to define the material constants files used for this MODE solutions calculation. These files are defined in Lumerical MODE software and are taken from the textbook by Palik [3] - plots of these constants files are given in Figure 5 and Figure 6. As can be seen by the materials index of refraction fitting, the cladding has very little dispersion, while the Si has dispersion to a much greater degree in the 1500nm-1600nm wavelength range being considered for this project. Both materials have

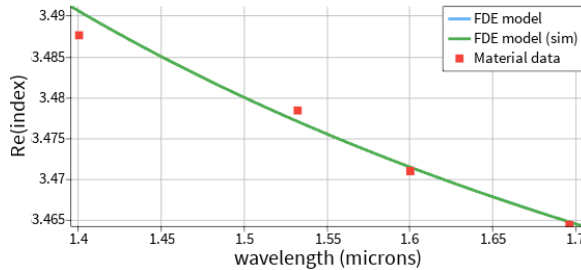


Fig. 5: Multi-coefficient model fit to Palik data on the varying index of refraction of Si with wavelength (dispersion).

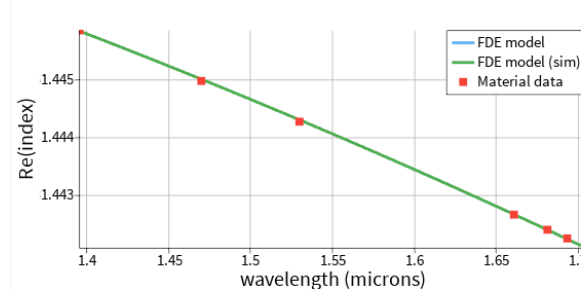


Fig. 6: Palik materials linear fit for SiO₂ cladding - very little dispersion.

negligible imaginary part of refractive index (less than 10^{-8}) in this wavelength range - loss due to material absorption will be relatively low.

For the purposes of providing a compact waveguide model, only the dominant TE mode will be investigated for 500nm wide and 220nm thick waveguides. The compact model for $w = 0.5\mu m$ with $\lambda_o = 1.55\mu m$ that we have found in this course is about:

$$n_{\text{eff}}(\lambda) = n_1 + n_2(\lambda - 1.55) + n_3(\lambda - 1.55)^2 \quad (2)$$

$$n_1 = 2.44, n_2 = -1.13, n_3 = -0.044$$

Using this model, the following is analytically true:

$$n_{\text{eff}}(\lambda_o) = n_1$$

$$n_g(\lambda) = n_1 - n_2\lambda_0 \text{ for } n_3(\lambda^2 - \lambda_0^2) \ll 1 \quad (3)$$

$$\frac{dn_g(\lambda)}{d\lambda} = -2\lambda n_3$$

where $n_g(\lambda)$ is the group index of the waveguide, and the derivative of the group index is especially correlated with the waveguide dispersion D . This waveguide dispersion can become more significant for quasi-TM mode analysis, but given that we are studying only quasi-TE mode analysis in this project, this dispersion will be relatively small ($n_3(\lambda^2 - \lambda_0^2) \ll 1$ in most cases).

Now we shall turn to the theory of the MZI and its FSR. It is worthwhile to provide a short derivation demonstrating the connection between the FSR and the group index.

First, it is noteworthy to consider that for the output signals of the MZI interferometer (the MZI will soon be shown in detail as an optical circuit in Lumerical Interconnect), there are “fringes” (sinusoidal signals) that encode information about the phase change of the two beam paths in the circuit setup. In this case, wavelength difference between adjacent peaks of the signal is called the Free Spectral Range (FSR) of the interferometer. The MZI has a transfer function expressed as the following:

$$\begin{aligned} \frac{I_o}{I_i} &= \frac{1}{4} |e^{-i\beta_1 L_1 - \frac{\alpha_1}{2} L_1} + e^{-i\beta_2 L_2 - \frac{\alpha_2}{2} L_2}|^2 \\ &\approx \frac{1}{2} e^{-\frac{\alpha_1 L_1 + \alpha_2 L_2}{2}} (1 + \cos(\beta_1 L_1 - \beta_2 L_2)) \quad (4) \\ &\text{for } \frac{\alpha_1 L_1 + \alpha_2 L_2}{2} \ll 1 \end{aligned}$$

where the first line of Equation 4 is found through studying the change in phase of the plane wave E-Field as the split input signals travel their (different) respective paths through space. Both a change in the propagation constant β_i and the path length L_i will result in a phase shift from one path to another. The total loss in the system is represented by the inverse idea - the path sum (rather than the difference) of the loss propagation constant multiplied by the path lengths L_1 and L_2 expresses the loss in the system. This idea makes sense since the loss constant is an average loss per unit length of the waveguide, so depends on the total length traversed by both signals. For these reasons, the interferometer is a good method for studying the properties of waveguides, as changes in either effective index or path length will produce changes to fringe patterns in both output signals that can be studied and related to the properties of the passive optical component (the waveguide). For the remainder of this discussion, we will neglect the loss term, which when converting the transfer function to dB units, corresponds simply to a vertical shift and does not provide information on path difference and group index of the waveguide. With exponential decay term neglected, this transfer function is clearly maximized (i.e. a peak arises) for a path length difference that follows the condition:

$$\beta_1 L_1 - \beta_2 L_2 = 2\pi m \quad (5)$$

If we assume that the waveguides are identical in terms of their optical index properties (i.e. $\beta_1 = \beta_2 = \beta = \frac{2\pi n_{\text{eff}}}{\lambda}$) such that only a path length difference $\Delta L = L_1 - L_2$ introduces a phase difference between the two beams, then for adjacent peaks in the output signal:

$$\Delta\beta = \frac{2\pi}{\Delta L} \quad (6)$$

Assuming that β varies linearly in the local region of a device with small FSR, we find that:

$$\begin{aligned}\Delta\beta &\approx -\Delta\lambda \frac{d\beta}{d\lambda} \\ \implies \Delta\lambda &\approx -\Delta\beta \left(\frac{d\beta}{d\lambda} \right)^{-1}\end{aligned}\quad (7)$$

where from Equation 6 we know:

$$\begin{aligned}\frac{d\beta}{d\lambda} &= \frac{2\pi}{\lambda} \frac{dn_{\text{eff}}}{d\lambda} - \frac{2\pi n_{\text{eff}}}{\lambda^2} \\ &= -\frac{2\pi}{\lambda^2} \left(-\lambda \frac{dn_{\text{eff}}}{d\lambda} + n_{\text{eff}} \right)\end{aligned}\quad (8)$$

Combining Equation 6, Equation 7, or Equation 8, we get:

$$\begin{aligned}\text{FSR} = \Delta\lambda &= \frac{\lambda^2}{\Delta L \left(n_{\text{eff}} - \lambda \frac{dn_{\text{eff}}}{d\lambda} \right)} \\ &= \frac{\lambda^2}{\Delta L n_g}\end{aligned}\quad (9)$$

And hence, we have related the group index n_g of the optical system to a measurable parameter of the output of the MZI. This is very useful and will be the topic of this report's investigation. However, before moving onto that, we will finish with a discussion of some modes of loss that we will consider in the analysis of the designed system. Note that for the FSR derivation discussed above, the loss could be hidden as an imaginary part of the index of refraction n , though the theory calculation above is ideal. Some sources of loss in the optical circuit are:

- losses from the grating couplers.
- losses (per unit length) in the waveguides.
- losses in the waveguide due to bends, which is influenced by the waveguide width.

III. DESIGN PROPOSAL

The MZI optical circuit as designed in Lumerical Interconnect is found in Figure 7 and Figure 8. The design in KLayout uses 5um bend radii recommended by the course for dominant TE mode. The bottom row interferometers in KLayout image are the width equals 500nm waveguides, while the top row is identical waveguides which will be used to gauge manufacturing variability. The two de-embedding circuits on the right side of the KLayout drawing are as follows: the bottom one is the grating couplers 500um waveguides, while the top one is an interferometer with no path length difference using 500um wide waveguides between Y-Branches. The ΔL values for the sets of five interferometer circuits are given in Table I and Table ???. Here, we are using S-parameter grating couplers coming out of the active network analyzer. The S-parameter file is the

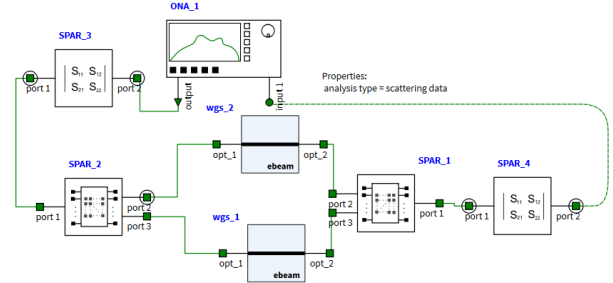


Fig. 7: The MZI design setup in Lumerical Interconnect.

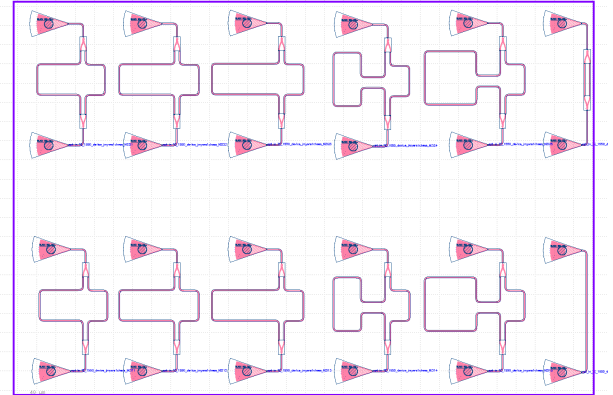


Fig. 8: The MZI design setup in KLayout.

“S_TE1550_SubGC_neg31_oxide.txt”. A non-ideal Y-Branch is used to split and combine the two beams. Note that for an ideal 50/50 Y-Branch splitter, the two component output of the intensity and electric field are:

$$I_{o1,2} = \frac{I_i}{2}, E_{o1,2} = \frac{E_i}{\sqrt{2}} \quad (10)$$

The ideal Y-Branch combiner is similarly for the dominant TE mode:

$$I_o = \frac{I_i}{4} |1 + e^{-i\beta\Delta L}|^2, E_o = \frac{E_i + E_{i2}}{\sqrt{2}} \quad (11)$$

The gain for the grating coupler and the non-ideal Y-Branch is given in Figures 9 and 10. As can be seen, there is some loss in the gain of the Y-Branch from the non-ideality of the component (gain is less than -3.01dB, so the split is not 50%-50%) - the file used is “S_YBranch.txt”. Then the split signals pass through the waveguides of varying length. The 1550nm E-beam strip waveguide from the compact model library was used for the FSR simulations. The shorter length waveguide will be 100um. The 6 waveguide lengths to be fabricated (with their associated FSRs) with width of 500nm is given in Table I. These FSRs can be compared to simulation of the group index and the theory formula given by Equation 9. For example, for $\Delta L = 100\mu\text{m}$,

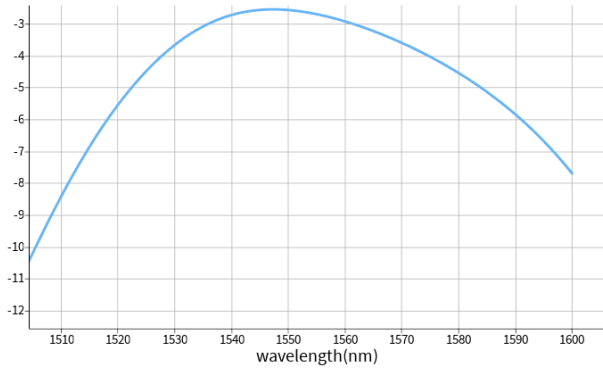


Fig. 9: The grating coupler gain. Graph y-axis is in dB.

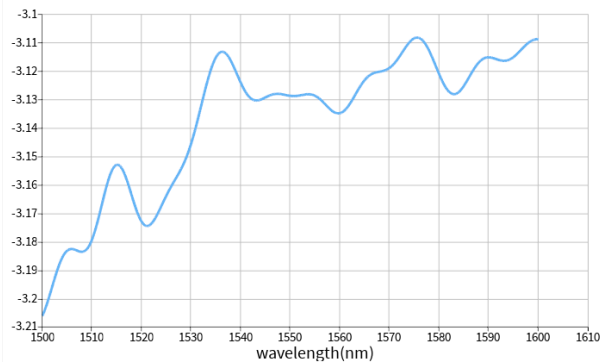


Fig. 10: The non-ideal Y-Branch gain. Graph y-axis is in dB.

for $n_g = 4.2$ at 1550nm, this gives an FSR of 5.7, in line with the simulated behaviour given by the results in Table I. The other FSRs in Table I roughly agree with Equation 9 for $n_g = 4.2$. The FSR will be obtained from experimental data by analyzing the distance between the fringes of the gain for each ΔL . Then, the gain experimental data will be fit by a parameterized transfer function to that encodes the compact model of the effective index, which can then be used to estimate the group index of the waveguide.

Finally, the simulated non-ideal gain is shown in Figure 11 for the MZI with $\Delta L = 100\mu m$. The simulated transmission spectrum for the waveguide with $\Delta L = 100\mu m$ is given in Figure 12.

As will be shown in the section analysing the experimental data, there is a wavelength dependent loss that can be attributed to the loss coefficient α_i per unit length of the waveguides, loss in the grating coupler and Y-Branch, as well as loss in the waveguide bends. However, when considering the data analysis methodology, the inclusion of this loss has only a small effect on the positioning of the peaks when fitting the transfer function to experimental data.

$\Delta L (\mu m)$	FSR (nm)
50	11.5
75	7.65
100	5.75
150	3.83
200	2.86

TABLE I: ΔL of simulated waveguide and FSR. The FSRs were taken from simulated data in Lumerical Interconnect. These agree well with Equation 9 for $n_g \approx 4.2$.

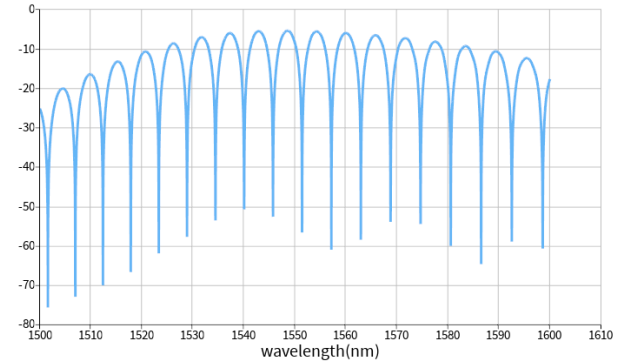


Fig. 11: The simulated MZI gain with $\Delta L = 100\mu m$.

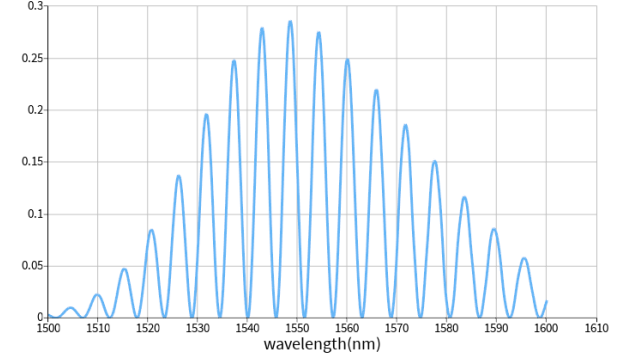


Fig. 12: The simulated MZI transmission spectrum (absolute valued squared) with $\Delta L = 100\mu m$.

IV. SIMULATING MANUFACTURING VARIATIONS

Next, we will discuss the experimental results that we may expect to get given typical manufacturing errors from the electron beam lithography process. This analysis will be carried out in the form of a set of monte carlo simulations done in MATLAB using interpolated results of Lumerical MODE solutions.

From course content, it is estimated that the the electron beam lithography process will produce waveguide dimensions with the following tolerances:

- mean waveguide thickness of 219.2nm, with a standard deviation of 3.9nm. It will be assumed that this standard is relatively constant within a single MZI,

as the circuits are well confined within KLayout, so uniformity variation will be relatively small.

- feature sizing mean between fabrication runs of +10nm to -30nm.
- feature sizing value within run variation of $\pm 10\text{nm}$ - a conservative estimate. To reflect the conservativeness of the within run variation, we will assign this $\pm 10\text{nm}$ variation as 2 standard deviations in a Gaussian distribution, or a tolerance that encompasses more than 95% of samples from this distribution.

Thus, we will run Monte Carlo simulations where:

- the waveguide thickness is sampled from a Gaussian distribution with a mean of 219.2nm and a standard deviation of 3.9nm.
- the waveguide mean width and length deviation from design for a given run is sampled from a uniform distribution with maximum value of +10nm and a minimum of -30nm.
- the waveguide width and length values vary about the run-to-run mean as a Gaussian distribution with a mean given by the run-to-run mean feature size (see Point 2 in this list) and a standard deviation of 5nm.

To carry out the Monte Carlo simulations, we first must attain effective index data between 1500 and 1600nm for waveguides of various thicknesses and widths reflecting the maximums and minimums common within the simulation. Thus, Lumerical MODE solutions were used to extract the effective index for the dominant quasi-TE mode for 2 standard deviations above and below the thickness mean, as well as 2 standard deviations above and below the range of possible width and length feature sizes. This led to 20 simulations in total, as thicknesses sampled were 211.4nm, 215.3nm, 219.2nm, 223.1nm, and 227nm, while the widths sampled were 460nm, 480nm, 500nm, and 520nm (where 460nm is the minimum width value within 2 standard deviations about the mean, while 520nm is the maximum width value within 2 standard deviations about the mean, and step sizes of 20nm provide good possibility for accurate interpolation). Once these parameter sweeps were determined, the data for each dataset were manipulated by fitting the 2nd degree Taylor series compact model (Equation 1) to each data set individually over 1500-1600nm. Then doing a linear regression for each n_1 , n_2 , and n_3 with varying thickness for each width. Then, the linear regressions over parameter value and thickness for each width are given in Figure 13, Figure 14, and Figure 15. All linear regressions for each parameter with changes in thickness for each width were $R^2 > 0.9$. As can be seen in Figure 13 and Figure 14, the n_1 and n_2 parameters in the compact model parameters linear fits as thickness varies are about uniformly separated and relatively parallel for each width. The n_3 parameter is

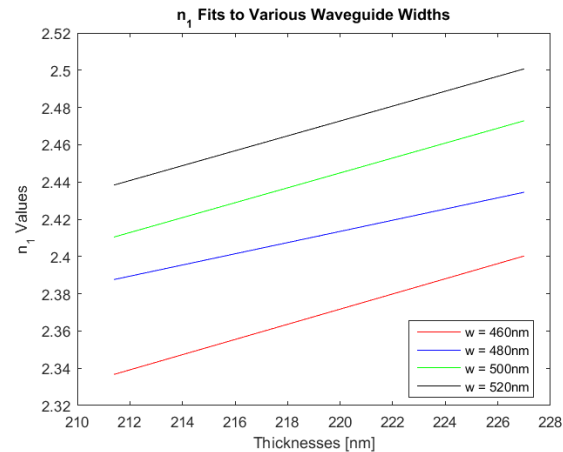


Fig. 13: The linear regressions to the thickness variable of the compact waveguide model n_1 for each width.

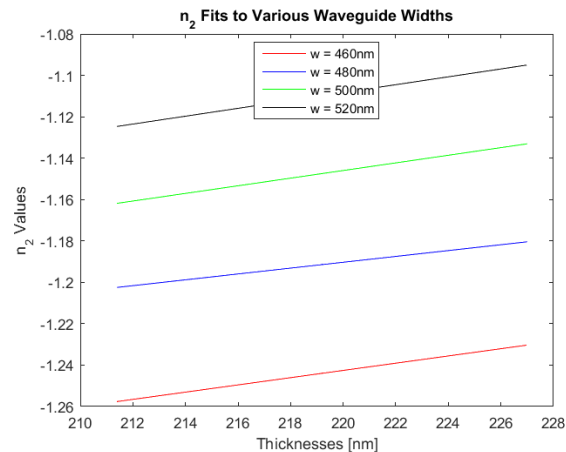


Fig. 14: The linear regressions to the thickness variable of the compact waveguide model n_2 for each width.

more complex relationship between widths, but it also has the least significant contribution to the value of the effective index. Thus, we will treat the 3 parameter models as accurately interpolatable between variable width and thickness appearing in the Monte Carlo simulation. Once these relationships are established, we can begin generating randomly varying waveguide thickness, width, and length values and then compute the simulated approximation to the system behaviour over a variable number of runs and a variable number of MZI in each run. Each MZI was computed to have two waveguides with different width and length variations about the intended design parameters. Due to the uniform run-to-run variation in mean feature sizing, the group index distribution n_g varies from simulation to simulation (1000 runs were analyzed, with 300 MZIs for each run), as can be seen by the results for two simulations in Figure 17

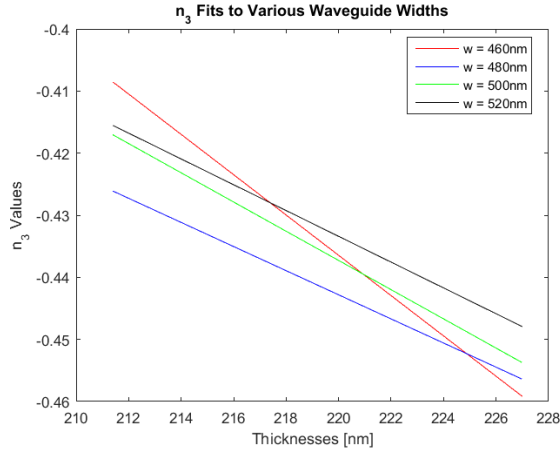


Fig. 15: The linear regressions to the thickness variable of the compact waveguide model n_3 for each width.

and 18. However, the FSR distribution is nearly identical for these two simulations. This observation is a notable consequence that for a large number of iterations, the distribution ΔLn_g is relatively similar from simulation to simulation, and appears to be nicely Gaussian shaped dependent on the target ΔL for the simulation. Thus, since ΔLn_g is generally Gaussian for large iterations, the distribution of the $FSR = \frac{\lambda^2}{\Delta Ln_g}$ is always nearly identical for a given simulation. This observation is noteworthy enough that we make a table of the expected distribution standard deviation of the FSR that we will compare against the results of the data analysis of our fabricated circuits (see Table II and Figures 19). As a summary of the algorithm used to compute these results, see Figure 16 for a skeleton of the algorithm used for the Monte Carlo Simulation. The simulation

Fig. 16: The skeleton of the algorithm for the Monte Carlo trials used to compute the FSR uncertainty expected from the experimental data from the fabrication run. This algorithm computes the FSR distribution at $\lambda = 1550\text{nm}$.

results in Table II yield non-symmetric FSR distributions (especially for smaller values of ΔL - see Figure 19), and thus give non-symmetric upper and lower tolerances.

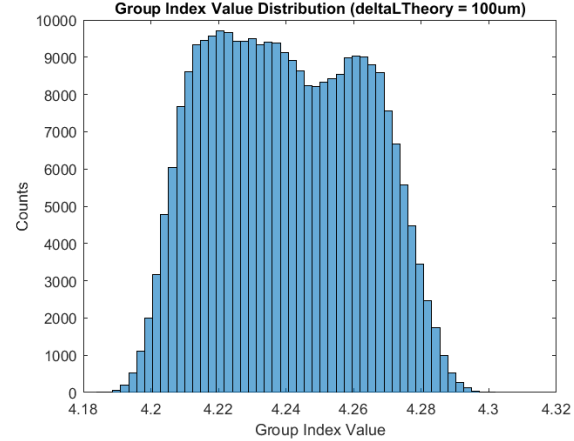


Fig. 17: One n_g distribution for $\Delta L = 100\mu m$ for 1000 manufacturing runs and 300 waveguides per run at a wavelength $\lambda = 1550\text{nm}$.

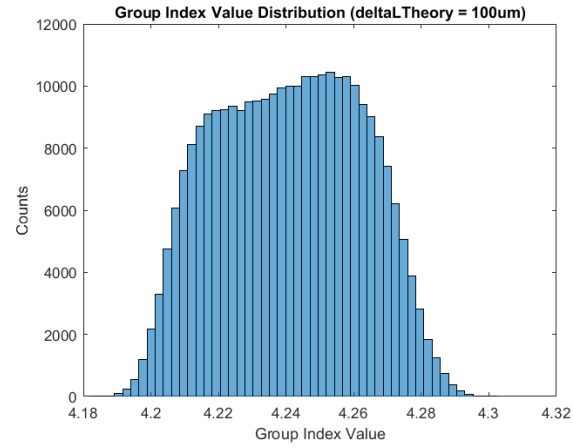


Fig. 18: A second n_g distribution for $\Delta L = 100\mu m$ for 1000 manufacturing runs and 300 waveguides per run at wavelength $\lambda = 1550\text{nm}$.

Next, we will compare these simulated results to the results obtained by analyzing experimental data.

V. FABRICATION OF MZI DESIGN

The photonic devices were fabricated using the NanoSOI MPW fabrication process by Applied Nanotools Inc. (<http://www.appliednt.com/nanosoi>; Edmonton, Canada) which is based on direct-write 100 keV electron beam lithography technology. Silicon-on-insulator wafers of 200 mm diameter, 220 nm device thickness and 2 μm buffer oxide thickness are used as the base material for the fabrication. The wafer was pre-diced into square substrates with dimensions of 25x25 mm, and lines were scribed into the substrate backsides to facilitate easy separation into smaller chips once fabrication was

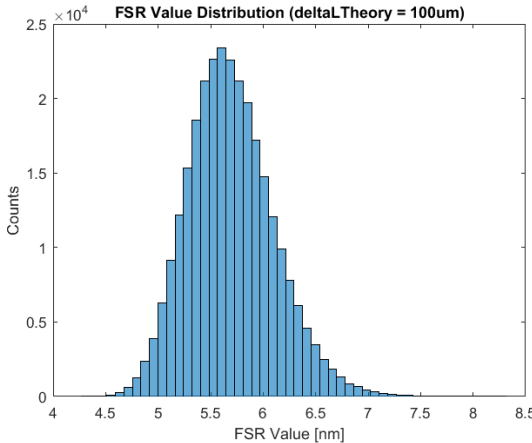


Fig. 19: The FSR distribution for $\Delta L = 100\mu m$. This distribution changes relatively little from simulation to simulation. This distribution has a mean and standard deviation as given in Table II, and corresponds to a wavelength of $\lambda = 1550\text{nm}$.

$\Delta L (\mu m)$	FSR (nm)
50	$10.63 + 2.48 - 1.86$
75	$7.345 + 0.98 - 0.78$
100	$5.61 + 0.53 - 0.44$
150	3.77 ± 0.21
200	2.83 ± 0.12

TABLE II: The FSR values for each ΔL given in Table I predicted by the Monte Carlo simulation. These values are for 100 manufacturing runs and 10000 waveguides fabricated per run, for a total of 1 million waveguides simulated. This FSR distribution corresponds to $\lambda = 1550\text{nm}$.

complete. After an initial wafer clean using piranha solution (3:1 H₂SO₄:H₂O₂) for 15 minutes and water/IPA rinse, hydrogen silsesquioxane (HSQ) resist was spin-coated onto the substrate and heated to evaporate the solvent. The photonic devices were patterned using a JEOL JBX-8100FS electron beam instrument at The University of British Columbia. The exposure dosage of the design was corrected for proximity effects that result from the backscatter of electrons from exposure of nearby features. Shape writing order was optimized for efficient patterning and minimal beam drift. After the e-beam exposure and subsequent development with a tetramethylammonium sulfate (TMAH) solution, the devices were inspected optically for residues and/or defects. The chips were then mounted on a 4" handle wafer and underwent an anisotropic ICP-RIE etch process using chlorine after qualification of the etch rate. The resist was removed from the surface of the devices using a 10:1 buffer oxide wet etch, and the devices

were inspected using a scanning electron microscope (SEM) to verify patterning and etch quality. A 2.2 μm oxide cladding was deposited using a plasma-enhanced chemical vapour deposition (PECVD) process based on tetraethyl orthosilicate (TEOS) at 300°C. Reflectrometry measurements were performed throughout the process to verify the device layer, buffer oxide and cladding thicknesses before delivery.

VI. MEASUREMENT DESCRIPTION

To characterize the devices, a custom-built automated test setup [4] [5] with automated control software written in Python was used [6]. An Agilent 81600B tunable laser was used as the input source and Agilent 81635A optical power sensors as the output detectors. The wavelength was swept from 1500 to 1600 nm in 10 pm steps. A polarization maintaining (PM) fibre was used to maintain the polarization state of the light, to couple the TE polarization into the grating couplers [4]. A 90° rotation was used to inject light into the TM grating couplers [7]. A polarization maintaining fibre array was used to couple light in/out of the chip [8].

VII. ANALYSING EXPERIMENTAL DATA

The experimental data analysis has multiple stages:

- Analyse and subtract out the gain of the grating coupler from the de-embedding photonic circuit.
- Carry out analysis to fit the transfer function to the data by determining the compact model for the effective index.
- Carry out a linear fit for the FSR vs. $\frac{1}{\Delta L}$ at $\lambda = 1550\text{nm}$ to determine the group index quantity as the slope of the regression equation. This approach represents a method for determining the justified, low uncertainty number considering the data from all the MZIs.

To fit the de-embedding circuits, we use a 4th degree polynomial fit. See Figure 20 for this fitting - the approach is intended to find a good fit between the noise. This fit is done only on the data that is above -30dB, to ensure that the fit is best in the middle of the spectrum between 1520nm and 1580nm. Then, this data is subtracted from each of the gain curves for the MZIs, where we assume that the grating couplers are identical for each circuit. Then, we carry out a moving average smoothing algorithm to the gain data to allow for the easy peak detection algorithm `findpeaks` in MATLAB to find the wavelength dependent FSR. An example of smoothed data for $\Delta L = 100\mu m$ is given in Figure 21. Then, the peaks were found. Now, to find the parameters of the 2nd order compact model of the effective index, we carry out the following algorithm.

- **Determining n_1 :** The exact value of n_1 is not very important, as n_1 only determines the horizontal shift

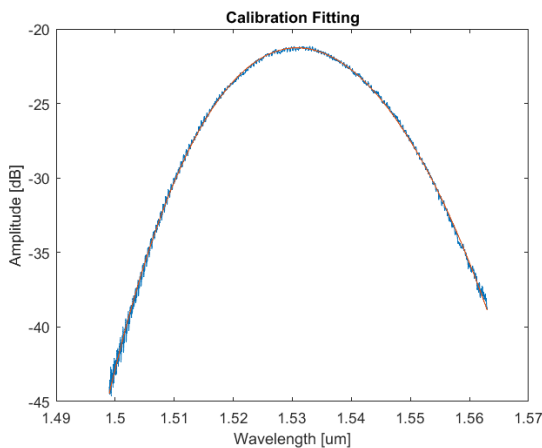


Fig. 20: The de-embedding circuit gain with 4th degree polynomial fitting.

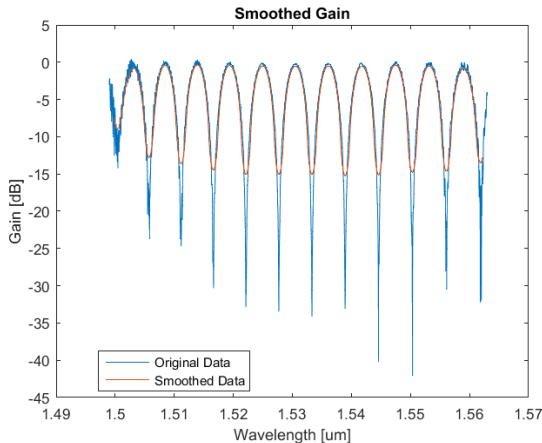


Fig. 21: The smoothed gain data plotted with the original gain data for $\Delta L = 100\text{um}$.

n_1 where the $\cos(\beta\Delta L) = 0$, or where $\frac{2n_{\text{eff}}\Delta L}{\lambda} = 2N + 1$, where N is a positive integer):

$$N = \text{round}\left(\frac{\tilde{n}_{\text{eff}}(\lambda_0)\Delta L}{\lambda_0} - \frac{1}{2}\right) \quad (12)$$

$$\implies n_1 \approx \frac{\lambda_0}{2\Delta L}(2N + 1)$$

In this scheme, we make an assumption of an approximate value of n_{eff} at the intermediate value of λ_0 (preferably a minimum near to the middle of the data spectrum, such as near $\lambda_0 = 1.55\text{um}$). For example, assume $\tilde{n}_{\text{eff}} = 2.4$.

- **Determining n_2 :** Determine $n_g(\lambda)$ through Equation 9 obtained by finding the FSR at $\lambda_0 = 1550\text{nm}$

by analysing the wavelength difference between the peaks in the experimental data, then carrying out a linear fit to the FSR data. Then we can determine $n_2 = -\frac{\tilde{n}_g - n_1}{\lambda_0}$ directly from Equation 3 solution for n_g (assuming that $n_3 (\lambda^2 - \lambda_0^2)$ is small).

- **Determining n_3 :** Then, we use observation from Equation 3 that the slope of the wavelength dependent derivative of the group index is:

$$\frac{dn_g}{d\lambda} = -2\lambda n_3 \quad (13)$$

Thus, by using the linear regression modelling the FSR for each λ , we can find the group index modelling for each λ through $n_g = \frac{\lambda^2}{\Delta L \cdot FSR(\lambda)}$. Then, we can use the numerical relation of $\frac{dn_g}{d\lambda} = \lim_{\Delta\lambda \rightarrow 0} \frac{n_g(\lambda + \Delta\lambda) - n_g(\lambda)}{\Delta\lambda}$. Then, we use Equation 13 to find n_3 from the slope of the numerical derivative of n_g with wavelength.

This methodology was used to fit the compact model to the experimental gain measurements for each MZI ΔL - an example fit for $\Delta L = 100\text{um}$ is given in Figure 22.

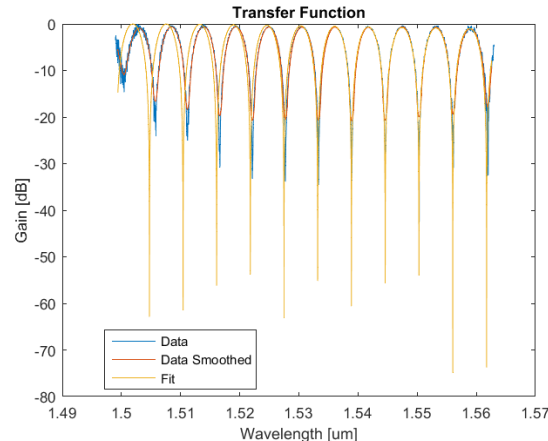


Fig. 22: The fitted gain data plotted with the original and smoothed gain data for $\Delta L = 100\text{um}$ for the compact model given in Table III.

In this example plot, we have guessed a loss value that increases linearly as we move towards higher wavelengths. This assumption seems to fit the experimental data nicely. The table of compact model parameter values for each MZI is given in Table III. In Table IV we summarize the results of the linear fittings of FSR vs. wavelength. Then, the FSR at $\lambda_0 = 1550\text{nm}$ was extracted from the fit to the data for each ΔL , and those results are also summarized in Table IV. One such fitting is given in Figure 23 for $\Delta L = 100\text{um}$.

The σ_{FSR} in Table IV is the standard deviation of the residuals of the linear FSR fit for each ΔL . The

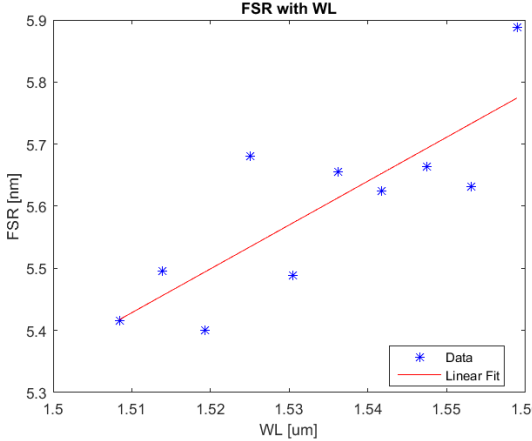


Fig. 23: The FSR vs. Wavelength for $\Delta L = 100\text{um}$ using a linear fit to the experimental data points determined through calculating the distance between the peaks.

$\Delta L [\text{um}]$	n_1	$n_2 [\text{um}^{-1}]$	$n_3 [\text{um}^{-2}]$
50	2.391	-1.192	-2.691
75	2.405	-1.171	-0.599
100	2.395	-1.168	-1.570
150	2.402	-1.160	-1.697
200	2.397	-1.155	-1.721

TABLE III: The compact model for each ΔL for a $\lambda_0 \approx 1.55\text{um}$.

FSR results are plotted in Figure reffig: with the second first and second columns of Table IV representing the 2D point coordinates and the third column of the table representing the vertical error bars for each point. We assume no horizontal error here, which is a reasonable assumption as we are plotting $\frac{1}{\Delta L}$ on the horizontal axis. The data has a straight line fit to it, with all five data points meeting the trend line within the error bars. This plot was used to carry out a Monte Carlo simulation with 10^5 weighted linear fittings (with the weights determined by $w_i \sim \frac{1}{e_i^2}$, where e_i is the vertical error bar value, and $\sum_i w_i = 1$). The random variable is a normally distributed vertical error variation that for each point proportional to the error bar magnitude for that point. The inverse error bar squared weightings seem appropriate as the point with most uncertainty on the right side of Figure 24 also has the fewest FSR peaks ($\Delta L \approx 50\text{um}$), and with variations in the data do not give as strong of a prediction as the data points with more FSR peaks (and substantially smaller error bars). Thus, the weighting gives the least weight to the $\Delta L \approx 50\text{um}$ point relative to the other points once scaled for normalization ($\sum_i w_i = 1$). The algorithm employed for these Monte Carlo trials is found in Figure 25, and is generally useful for determining the uncertainty on the

$\Delta L [\text{um}]$	$FSR [\text{nm}]$	$\sigma_{FSR} [\text{nm}]$
50	11.37	0.37
75	7.59	0.05
100	5.71	0.09
150	3.81	0.04
200	2.87	0.04

TABLE IV: FSR values for each ΔL value for $\lambda = 1.55\text{um}$. All of these values are within the expected range of values given by the Monte Carlo simulations (see Table II).

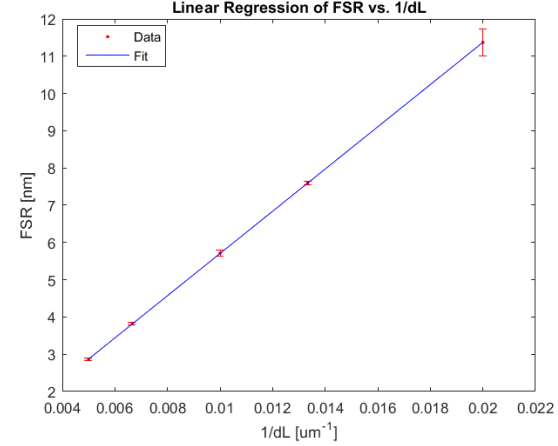


Fig. 24: The FSR plot vs. $\frac{1}{\Delta L}$ used to determine the slope and the corresponding best estimate of n_g at $\lambda = 1.55\text{um}$. This plot has an $R^2 = 0.9999$ (an acceptable, quality fit).

best estimate for the group index. With the 10^5 Monte Carlo simulations, the best estimate was determined by the following formulas:

$$\tilde{n}_g = \text{mean}(n_{g\text{sim}}) \quad (14)$$

$$\delta\tilde{n}_g = \text{std}(n_{g\text{sim}})$$

```

8 %Model Parameters
9 M = 1000000
10
11 %Defining Plot Vectors
12 xdata = 1/(1.36975536427*5.926744795*7.134674717*3.81468025882*0.899325490); %um^-1
13 ydata = [11.36975536427*5.926744795*7.134674717*3.81468025882*0.899325490]; %nm
14 errorbar = [0.36563701*0.0517460.0.090409*0.036519*0.036240];
15
16 %Looping for Monte Carlo Effects
17 ngsimDev = zeros(M,1)
18 for i=1:M
19     %Generating Random Error Variation
20     ydataSim = zeros(length(ydata),1);
21     for j = 1 : length(ydata)
22         ydataSim(j) = ydata(j) + errorbar(j)*randn;
23     end
24     weight = (1./errorbar).^2*(sum(1./errorbar.^2));
25
26     %Performing Linear Regression on Plotted Data
27     xmean = sum(weight.*xdata)/sum(weight);
28     ymean = sum(weight.*ydata)/sum(weight);
29     mlope = sum(weight.*((xdata - xmean).*((ydataSim - ymean)).^2));
30     yint = ymean - mlope*xmean;
31     ypred = mlope*xdata + yint;
32     h = plot(xdata,ydata,'*r',xdata,ydataSim,'*b');
33
34 %Calculating Group Index
35 ngsimDev(i) = 1.55^2/mlope*1e3;
36 ngsimDev(i) = abs(1.55^2/mlope*1e3*mean);
37 mag = 1 - sum(weight.*ypred - ydata).^2/sum(weight.*(ymean - ydata).^2);
38 if mag < 1 = 1.0171*mag;

```

Fig. 25: The Monte Carlo algorithm used to determine the best estimate for the group index of the silicon waveguides at $\lambda = 1.55\text{um}$ in the fabricated designs that are the topic of this report.

So the corresponding best estimate of the group index after the Monte Carlo simulations at $\lambda = 1.55\text{um}$ is: $n_g(\lambda = 1.55\text{ um}) = 4.239 \pm 0.053$. This value and uncertainty was consistent to the 3 decimal across several simulations.

VIII. DISCUSSION

Now that we have done the analysis for the report, it seems worthwhile to evaluate the insights that we can draw from the data. For instance, it seems prudent to raise the question: why did the Section IV Monte Carlo simulation provide changing distributions of group index but the Monte Carlo simulation in Section VII has a tightly toleranced best estimate for n_g ? This question seems to be answered by examining the idea that FSR is a quantity that is relatively insensitive to manufacturing variations (as evidenced by the consistent distribution shape in Section IV), and if we then assume that the ΔL horizontal error bars in Figure 24 are 0um, then we find that the n_g derived using the method of Equation 9 from the slope of the linear regression must also be relatively insensitive to manufacturing errors, since it only depends on FSR and ΔL . However, the method used to yield the best estimate for the group index at $\lambda = 1.55\text{um}$ varies substantially from the method used to estimate n_g in Section IV, where we found n_g by interpolating between Lumerical MODE Solutions for n_{eff} and then calculating using Equation 3. Furthermore, by deriving the entire set of quantities by starting with the insensitive FSR quantity in the experimental data, we obtain substantially less uncertain answer for the group index than is seen when referring to Figure 17 and Figure 18.

One particularly interesting point of discussion is while the FSR linear fit gave relatively small error bars in the Figure 24 as the standard deviation of the RMS residuals, the exemplar linear fit in Figure 23 demonstrated a far more noisy distribution of data calculated from finding the distance between the peaks of the experimental data. The question then is easy to pose: are the small error bars for the leftmost 4 points in Figure 24 justified? To investigate this question, we will rerun a Monte Carlo simulation with larger error bars (as given in Figure 26) for all the points for 10^5 iterations. We find that the alternative best estimate to be: $n_g(\lambda = 1.55\text{ um}) = 4.253 \pm 0.233$, corresponding to only a 0.330% difference in the best estimate value but with a much larger tolerance. But of course with the addition of many more peaks for the $\Delta L = 200\text{um}$ FSR fit relative to the $\Delta L = 50\text{um}$ FSR fit, it is sensible for the leftmost points to have smaller error bar tolerances than the rightmost points. Furthermore, even if somewhat greater experimental error is possible for n_g at $\lambda = 1.55\text{um}$ than ± 0.053 , it seems reasonable to suggest the best estimate is fairly accurate to the true

value, and that the uncertainty on this value is potentially less well determined. It would be interesting to carry out an experiment with more distinct MZIs such that more ΔL points would be available to provide for a more precise estimate of n_g .

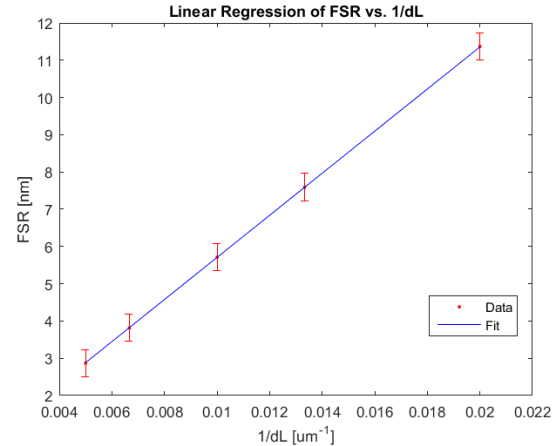


Fig. 26: The Monte Carlo simulation for the best estimate of group index done with large error bars on every point.

Finally, one may be wondering about why the top circuits in Figure 8 were ignored in the data analysis. These were MZIs that had an alternative width of 650nm rather than the conventional 500nm wide waveguides analysed in this report. However, after having submitted this design to the foundry, I decided that it would be best to limit the scope of the report to discussing the data from the 500nm wide waveguides, as these constrain the light to a single fundamental TE mode and already provide a great deal of interesting analysis and discussion. In future work, it would be interesting to make use of the additional top row of space to add more MZIs with changes in the ΔL to add more data points to the Figure 24 analysis. One important point to note however is that adding higher path difference waveguides will not add substantially more accuracy to the best estimate as the x-range of the plot with $\frac{1}{\Delta L}$ is only extended by a small margin (as $\Delta L \gg 1$). However, adding more MZIs with $\Delta L < 50\text{um}$ also seems undesirable as the limited measurement span only allows for a limited number of peaks, which will lead to an FSR estimate that is less well-determined for that point (with relatively large error bars). With this said, it seems most prudent to add some MZIs that are between $100\text{um} < \Delta L < 300\text{um}$ to both increase the range of $\frac{1}{\Delta L}$ and add more points to constrain the uncertainty of the linear fit in determining the best estimate for group index.

Finally, we found that the FSR values given in Table IV agree within the specified tolerance with the simulated

values in Table II. In fact, the agreement between the results in these two tables suggests that the manufacturing errors simulated in Section IV are likely too conservative - though this report does not investigate deeply, it would be worthwhile to investigate which parameters in the manufacturing variation Monte Carlo simulations could be realistically tightened to more accurately describe the degree of expected variation from simulated mean FSR values.

IX. CONCLUSION

In this study, we carried out a theoretical and experimental approach to find the best estimate of the group index of 219.2nm by 500nm silicon waveguides by creating 5 MZIs with varying path length differences. We begin by fundamentally describing electromagnetic propagation through silicon waveguides in the form of images from Lumerical MODE Solutions. We then progress to describe the compact model of the waveguide and to define the FSR of the MZI and its relation to the group index of the silicon waveguide in the MZI. We then carry out a procedure using Monte Carlo analysis to examine the impact of manufacturing errors on the expected experimental outputs. This analysis allowed us to define an expected value with a tolerance for the FSR of the MZI for each ΔL . After fabricating the silicon chip, the measurement data was analyzed to fit the transfer function for the MZI to the experimental data by determining the effective index 2nd order polynomial compact model. Then, the data from all 5 MZIs was compiled to attain a best estimate for the group index at $\lambda = 1.55\mu\text{m}$. All best estimates of FSR agree within the expected range of values from the Monte Carlo analysis. The best estimate of the group index is $\tilde{n}_g = 4.239 \pm 0.053$. As is evidenced by the agreement of the expected and experimental values within the report, this experimental process of estimating the group index via analysing the FSR seems quite repeatable and robust. Future work would fabricate more MZIs with different path length differences to give a more accurate and precise best estimate by having more ΔL points with smaller error bars.

X. ACKNOWLEDGEMENTS

I/We acknowledge the edX UBCx Phot1x Silicon Photonics Design, Fabrication and Data Analysis course, which is supported by the Natural Sciences and Engineering Research Council of Canada (NSERC) Silicon Electronic-Photonic Integrated Circuits (SiEPIC) Program. The devices were fabricated by Richard Bojko at the University of Washington Washington Nanofabrication Facility, part of the National Science Foundation's National Nanotechnology Infrastructure Network (NNIN), and Cameron Horvath at Applied Nanotools,

Inc. Omid Esmaeeli performed the measurements at The University of British Columbia. We acknowledge Lumerical Solutions, Inc., Mathworks, Mentor Graphics, Python, and KLayout for the design software.

REFERENCES

- [1] Zhoufeng Ying, Chenghao Feng, Zheng Zhao, Shounak Dhar, Hamed Dalir, Jiaqi Gu, Yue Cheng, Richard Soref, David Z Pan, and Ray T Chen. Electronic-photonic arithmetic logic unit for high-speed computing. *Nature communications*, 11(1):2154, 2020.
- [2] Lian-Wei Luo, Noam Ophir, Christine Chen, Lucas H Gabrielli, Carl B Poitras, Keren Bergman, and Michal Lipson. Simultaneous mode and wavelength division multiplexing on-chip. *arXiv preprint arXiv:1306.2378*, 2013.
- [3] Edward D Palik. *Handbook of optical constants of solids*, volume 3. Academic press, 1998.
- [4] Lukas Chrostowski and Michael Hochberg. *Silicon photonics design: from devices to systems*. Cambridge University Press, 2015.
- [5] Maple leaf photonics, seattle wa, usa. <http://mapleleafphotonics.com>.
- [6] Using python code developed by michael caverley. <http://siepic.ubc.ca/probestation>.
- [7] Yun Wang, Xu Wang, Jonas Flueckiger, Han Yun, Wei Shi, Richard Bojko, Nicolas AF Jaeger, and Lukas Chrostowski. Focusing sub-wavelength grating couplers with low back reflections for rapid prototyping of silicon photonic circuits. *Optics express*, 22(17):20652–20662, 2014.
- [8] Plc connections, columbus oh, usa. www.plcconnections.com.